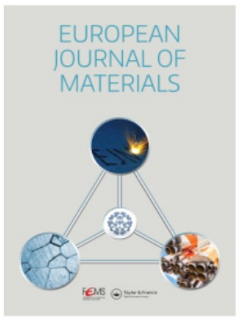

European Journal of Materials

ISSN: (Print) (Online) Journal homepage: https://www.tandfonline.com/loi/tems20

Effect of printing parameters on sintered WC-Co components by binder jetting

Marco Mariani, Davide Mariani, Gian Pietro De Gaudenzi & Nora Lecis

To cite this article: Marco Mariani, Davide Mariani, Gian Pietro De Gaudenzi & Nora Lecis (2022) Effect of printing parameters on sintered WC-Co components by binder jetting, European Journal of Materials, 2:1, 365-380, DOI: 10.1080/26889277.2022.2076617

To link to this article: https://doi.org/10.1080/26889277.2022.2076617

Published online: 26 May 2022.

EUROPEAN JOURNAL OF MATERIALS
2022, VOL. 2, NO. 1, 365–380
https://doi.org/10.1080/26889277.2022.2076617

Routledge
Taylor & Francis Group

Effect of printing parameters on sintered WC-Co components by binder jetting

Marco Mariani[a], Davide Mariani[a], Gian Pietro De Gaudenzi[b], and Nora Lecis[a]

[a]Department of Mechanical Engineering, Politecnico di Milano, Milano, Italy; [b]HI.Lab, FILMS S.p.A. - OMCD Group, Anzola d'Ossola, Italy

ABSTRACT

Hardmetals are materials employed to produce cutting and forming tools as well as wear resistant parts. Standard powder metallurgy suffers limitations in the manufacturing of shapes required by application-oriented design. Therefore, there is interest for the implementation of additive manufacturing, in particular low temperature techniques as binder jetting because they allow to preserve microstructures and peculiar properties. In our work, the powder was tungsten carbide with 12 wt.% cobalt (WC-Co). Shaping by binder jetting was followed by curing treatment to promote the binder polymerization, vacuum sintering and sinter-HIP to achieve near-full density. The powder was analysed in terms of size and shape, to determine its suitability for the procedure. Then, the effects of different combinations of printing parameters, layer thickness (50–100 µm) and binder saturation (60/75/90%), on the density of the green bodies were analysed. Finally, the relative density of the sintered components was measured and the pores shape and size were studied by SEM imaging, to assess possible consequences of the deposition procedure. Vickers hardness along the samples cross-section was measured and correlated to the printing conditions employed.

ARTICLE HISTORY
Received 15 October 2021
Accepted 9 May 2022

KEYWORDS
Cemented carbides; binder jetting; additive manufacturing; WC-Co; layer thickness; binder saturation

1. Introduction

The need of components with specific and complex geometries from hardmetals and cemented carbides has gathered the attention of the academy and the industry on the adoption of additive manufacturing

CONTACT Marco Mariani marco.mariani@polimi.it Department of Mechanical Engineering, Politecnico di Milano, Milano, Italy.

(AM) techniques applied to this class of materials. Indeed, the freedom of design granted by this kind of processes could allow for the commercialisation of customised products, with short production times, reduced costs and waste, and limited or no need for additional operations to adjust the size and shape by post-processing, which is challenging due to the high hardness and brittleness of cemented carbides (Aramian, Razavi, Sadeghian, & Berto, 2020; Gao et al., 2015; Lehmann & Zaeh, 2019; Lin, Xu, Shan, Chung, & Park, 2015; Seharing, Azman, & Abdullah, 2020).

At first, many efforts have been spent on employing this type of materials with more consolidated AM techniques, as selective laser sintering (SLS) and laser-powder bed fusion (L-PBF) (Campanelli, Contuzzi, Posa, & Angelastro, 2019; Chen et al., 2019; Grigoriev, Tarasova, Gusarov, Khmyrov, & Egorov, 2019; Ku, Pittari, Kilczewski, & Kudzal, 2019), laser engineered net-shaping (LENS) (Davoren, Sacks, & Theron, 2020) and direct metal laser sintering (DMLS) (Gu et al., 2012; Wang et al., 2002); however, the low control on the heating and cooling rates involved leads to a series of issues (e.g. thermal cracks, distortions, residual porosities, undesired carbides formation…) that prevent the quick adoption of these kind of processes, at least with current technologies and materials composition.

In the last years, indirect AM techniques, as fused deposition modeling (FDM) and binder jetting (BJ), have been extensively explored because they offer the advantages of application-oriented design combined to the possibility of controlling the thermal treatments required for the densification of the powders or granules employed. This allows to achieve a much tighter control on the microstructural evolution and retain a fine and homogeneous size distribution of equiaxed grains, with extremely limited amount of undesired phases and porosity (Cramer et al., 2020; Eguiluz, Ferr, Yus, & Ferrari, 2021; Enneti & Prough, 2019b; Lengauer et al., 2019; Mariani, Beltrami, et al., 2021; Mostafaei, De Vecchis, Kimes, Elhassid, & Chmielus, 2021; Mudanyi et al., 2021).

Although first attempts have displayed promising results, further research is needed to assess the effects of printing parameters on the final microstructural and mechanical properties. Currently, two types of WC-based powders have been employed in BJ, namely granulated (Carreño-Morelli, Alveen, Moseley, Rodriguez-Arbaizar, & Cardoso, 2020; Enneti et al., 2018; Enneti & Prough, 2019a, 2019b; Lehmann & Zaeh, 2019; Mostafaei, De Vecchis, et al., 2021) and fully dense feedstocks (Cramer, Nandwana, Lowden, & Elliott, 2019; Cramer, Nandwana, et al., 2019; Cramer et al., 2020; Cui et al., 2021; Mariani, Beltrami, et al., 2021; Mudanyi et al., 2021). The latter group comprehends works were BJ was

employed to produce preform, which were subsequently infiltrated with binder metal, as in Cramer et al. and Mudanyi et al., and one previous study of our group that features plasma spheroidised particles. Few studies have been realised on the effects of printing parameters, in particular:

- Enneti and Prough (2019a) observed the relevancy of layer thickness and binder saturation, rather than binder set time, on the properties of green samples (sintering was not performed);
- Mostafaei, De Vecchis, et al. (2021) described the effect of multiple parameters on green and densified components, obtained from powders produced by spray drying.

In our work, we explore the possibility of producing accurate and performing WC-Co components by binder jetting from a pre-densified feedstock. Specifically, an investigation on different combinations of layer thickness and binder saturation levels is presented, and the direct correlation of these two parameters to the organic binder distribution within the printed component, which has been demonstrated to affect the geometrical accuracy, the amount of residual carbon after debinding and the presence of excess porosity, among other effects (Enneti & Prough, 2019a; Mostafaei, De Vecchis, et al., 2021; Nandwana, Kannan, & Siddel, 2020).

2. Materials and methods

2.1. Materials and powder characterisation

WC - 12 wt.%Co powder by Global Tungsten & Powders Corp. (US) was employed, as in previous studies (Enneti et al., 2018; Mariani, Beltrami, et al., 2021). The raw material is plasma spheroidized to ensure a high shape regularity and it features a monomodal size distribution with a reduced average diameter (D_{50} = 1.5 µm, from the numerical distribution). The commercial aqueous-based binder "AquaFuse" by ExOne Inc. (US) was employed for all the printing campaigns.

Static image granulometry (ASTM E2651-19) was employed to determine the corresponding diameter and circularity degree of the particles from their 2D section projection. Circularity is calculated as the ratio of the circumscribed perimeter on the real perimeter of the particle. These features were confirmed by field emission-scanning electron microscopy (FE-SEM) with a ZEISS SIGMA 500. In addition, material composition was assessed by EDX analysis on a sufficiently large number of particles.

The packing and flowability behaviour of the powder was evaluated with a FT4 Powder Rheometer 2 (UK) by measuring:

- the apparent density (ρ_{app}), corresponding to that of the as-poured material;
- the tapped density (ρ_{tap}), i.e. the density after compaction by tapping the as-poured powder.

These values allowed to measure the Hausner ratio H, according to Eq. 1:

$$H = \rho_{tap} / \rho_{app} \tag{1}$$

2.2. Printing procedure

Components were produced with an Innovent + printer by ExOne Inc. (US). The machine parameters (listed in Table 1) affecting the deposition and spreading of the powder on the printing plate were optimised to assure the reliable formation of the layers throughout the whole printing process. The drying time was kept fixed at 12 seconds. Instead, five combinations of layer thickness (LT) and binder saturation (BS) were tested to assess their effect on the geometrical accuracy and density of the components at the green and sintered stages. In detail, LT was set at 50 µm or 100 µm and BS was 60%, 70% or 90%. BS of 90% immediately showed unsatisfying results, therefore it was tested only with 100 µm of LT. Samples nomenclature is given in Table 2.

Then curing was performed at 180°C for 6 hours in a static air oven to produce resistant green bodies, which underwent depowdering by manual brushing. Debinding was performed at 500 °C for 4 hours in inert

Table 1. Values of the parameters affecting deposition and spreading of the powder.

Recoat speed/mm s^{-1}	300
Roller speed/rpm	500
Drying time/s	12
Ultrasonic intensity/%	25
Powder hopper mesh size	200

Table 2. Combinations of layer thickness (LT) and binder saturation (BS) tested with the corresponding sample designation.

		LT/µm	
		50	**100**
BS/%	**60**	50_60	100_60
	75	50_75	100_75
	90	–	100_90

atmosphere and sintering at 1400 °C in vacuum. Finally, a sinter-HIP process was realised with a 35 bar pressure at 1400 °C for 20 minutes.

2.3. Microstructural and mechanical characterization

The relative density of the samples was calculated at all the steps of post-processing to evaluate the effect of the thermal treatments on the microstructure and accuracy. After curing density was measured by geometrical method given the large network of open porosity and samples brittleness, while Archimede's method was applied to sintered and sinter-HIPed specimens (ASTM B311-17). In both cases, the reference density considered for WC with 12 wt.% of Co was 14.29 g cm^{-3}.

The carbon content in all samples was measured by IR spectroscopy with a LECO WC230 according to ISO 11873. Sintered and sinter-HIPed microstructural features, as internal porosity, grain size and phase composition, were analysed by optical microscopy and FE-SEM on polished surfaces. The images were employed for analysis and manipulation by ImageJ through the trainable WEKA segmentation plugin to collect additional information on pores distribution with a resolution corresponding to 1 µm (Arganda-Carreras et al., 2017).

3. Results and discussion

3.1. Powder characterization

Granulometry (Figure 1) revealed that most of the particles stand in the 700 nm–10 µm range, thus the particles size distribution is shifted toward reduced diameters with respect to those usually employed in binder jetting and other additive techniques, which can go up to 100 µm (Mostafaei, De Vecchis, et al., 2021). This should ensure an optimal packing, as well as sintered density and geometrical accuracy, since the inter-particles porosity normally stands in the same size range.

A distinction was observed between the coarser fraction of the particles (diameter above 700 nm) that features a relevant circularity, consistently higher than 0.7, and the finer fraction (diameter below 400 nm), which displays a minimal shape homogeneity. Indeed, the latter fraction comprehends detected particles with a circularity degree below 0.3, meaning that the shape is elongated. These should be fragments that have detached from the main spheroidized particles during powder handling. SEM image of the as-receive powder in Figure 2 confirms the observations made on particles size and shape from granulometry. Fragments are visible in some spots (e.g. upper side of Figure 2).

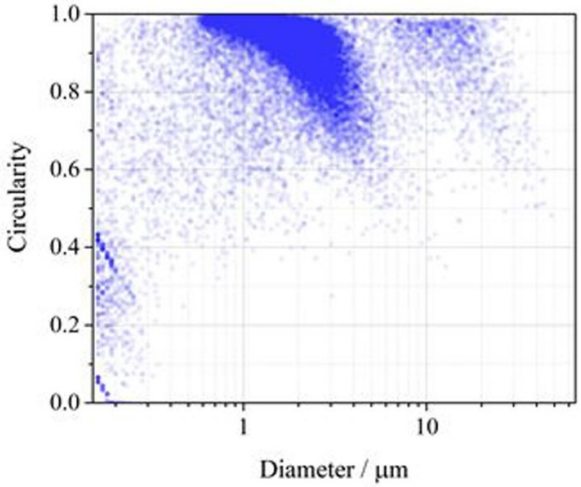

Figure 1. Circularity and size distribution of the individual particles elaborated from granulometric analysis.

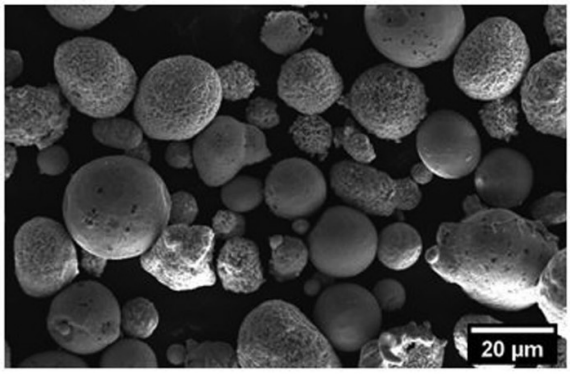

Figure 2. SEM image of the as-received powder.

Powder rheometry revealed that the employed material features an excellent flowability, considering that the Hausner ratio for a liquid would be 1.0. The result in Table 3 is impressive for such size distribution, and it is likely due to three main factors:

- accentuated sphericity of the particles
- high particles true density
- high hardness of the material

These features prevent particles mechanical interlocking and allows frictionless motion under their own weight without the need of powder de-humidification or similar operations, which is convenient in terms of time and cost.

3.2. Green specimens characterization

The printing parameters revealed to be highly influential on the repeatability and the accuracy of the process. Indeed, average density values display a limited variation in between the five combinations considered, ranging from 47.3% for 50_60 to 50.9% for 100_90, all of them being close to the powder packing value obtained by rheometric measurements in Table 3; however, the values distributions exhibit much different behaviours, as shown in Figure 3. The increase in average density with larger BS can be ascribed to the weight contribution of the binder itself, whereas the values distribution are correlated to the dimensional accuracy.

BS is the most influential parameter, particularly when combined with a larger LT (Rishmawi, Salarian, & Vlasea, 2018). It must be considered that the same BS level does not correspond to the same deposited binder volume at each layer with variable LT, as the volume to be filled increases with this parameter. Indeed, BS is defined as follows (Eq. 2):

$$BS = V_{db} \,/\, V_{por} \tag{2}$$

where V_{db} is the volume of binder deposited and V_{por} is the volume of the powder bed porosity. The latter parameter can be calculated as (Eq. 3):

$$V_{por} = (1 - PPR) * V_{sl} = \left(1 - PPR\right) * LT * S_{pgs} \tag{3}$$

where PPR is the powder packing ratio, V_{sl} is the single layer volume and S_{pgs} is the surface of the printed geometry section. Eq. 2 and Eq. 3 can be combined to calculate the volume deposited at each layer, as described in Eq. 4 and Eq. 5:

$$V_{db} = BS * V_{por} = BS * \left(1 - PPR\right) * LT * S_{pgs} = k_{p-g} * BS * LT \tag{4}$$

Table 3. Relative apparent density (%), tapped density (%) and Hausner ratio (H) of the as-received powder.

ρ_{app}/%	ρ_{tap}/%	H
50.69 ± 0.01	51.46 ± 0.01	1.02 ± 0.01

$$V_{db} * k_{p-g}{}^{-1} = BS * LT \tag{5}$$

where $k_{p\text{-}g}$ is a factor that depends on the powder packing ratio (material feature) and the printed geometry (system feature), which were constant in our case. The V_{db} ratios of our printing conditions are listed in Table 4.

Therefore, the amount of binder deposited at each layer for the five samples varies even when BS is the same. Ideally, the binder should be sufficient to equally fill the layer porosity and join the particles with the precedent layer; however, the wetting phase is deposited on the top surface of the layer regardless of its thickness, thus oversaturation may not be expected overall, but it might occur locally. This mechanism could lead to wetting out-of-bounds particles, due to capillarity in all directions, also sideward, thus reducing the printed shape accuracy, rather than

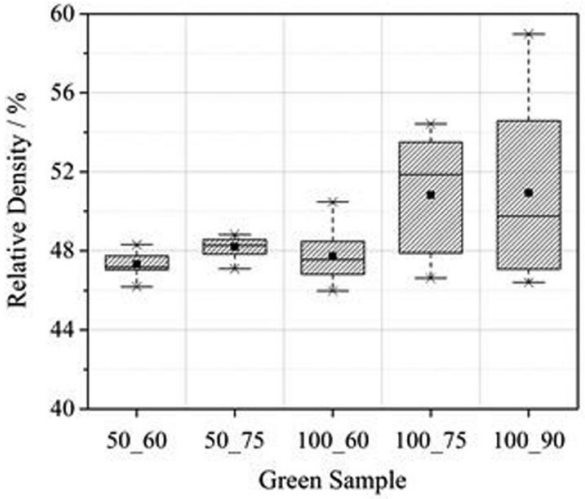

Figure 3. Relative density distributions of the green samples obtained from the combination of LT = 50/100 µm and BS = 60/75/90%.

Table 4. Ratios of the deposited binder volumes on the powder packing–geometry constant ($V_{db}\ k_{p\text{-}g}{}^{-1}$) for the five printing parameters combinations employed.

LT/µm	BS	$V_{db}\ k_{p\text{-}g}{}^{-1}$
50	0.60	30
50	0.75	37.5
100	0.60	60
100	0.75	75
100	0.90	90

completely infiltrate along the Z-axis (Chun et al., 2020; Mariani, Beltrami, et al., 2021). The risk of incomplete infiltration, thus of insufficient wetting at the layer-layer interfaces, with larger LT and same BS seems to be confirmed by the reduction in green strength measured by Enneti and Prough (2019a), under similar conditions, and by other studies on different materials (Barthel, Janas, & Wieland, 2021; Jimenez et al., 2019; Lecis et al., 2021; Mao, Li, Li, Cai, & Wei, 2021).

Consequently, the printed volume varies with respect to the desired geometry and this mechanism is accentuated when the overall liquid amount is higher, which occurs with an increase of either BS or LT or both. The limited control on the green samples geometry, when a larger volume of binder is employed, is responsible for the lower repeatability of the 100_75 and 100_90 printing combinations, as also observed by Mostafaei, De Vecchis, et al. (2021).

3.3. Sintered and sinter-HIPed specimens characterization

The sintering process allowed to achieve above 95% relative density values regardless of the printing conditions. As shown in Table 5, the densification degree was differentiated and varies inversely with the average relative density of the corresponding green specimens. In particular, the samples produced with BS = 60% experienced a densification of almost 50% and featured the largest density values. The amount and the distribution of the binder within the printed structure affects the characteristics of the samples: as already described in previous works, localised oversaturation may generate inhomogeneous and enlarged porosity after debinding, which hinders or reduces pores filling from solid-state or liquid-state diffusive mechanisms.

Sintering also has the beneficial effect of producing more homogeneous samples. This should be due to the overall reduction of the porosity, which is mostly of spherical shape, as the process achieve final stage sintering (Rishmawi et al., 2018). Pore size distributions and circularity (Figure 5) obtained from 2D transverse sections (examples are shown in Figure 4) confirm that meaningful differences in between samples are not detected. Therefore, the effect of irregular macro-porosities generated by improper binder distribution is mitigated. Samples with BS of 60%

Table 5. Average relative density (%) and densification degree (%) after sintering.

Sample	50_60	50_75	100_60	100_75	100_90
Avg. relative density/%	96.5 ± 0.1	95.8 ± 0.2	97.4 ± 0.2	96.0 ± 0.3	96.4 ± 0.3
Densification degree/%	49.2 ± 0.6	47.6 ± 0.5	49.6 ± 1.3	45.2 ± 2.9	45.4 ± 4.4

feature slightly larger average pore size, which could be due to the more progressed sintering process leading partially to porosity coalescence.

Sinter-HIP revealed to be a fundamental step in the process since it increased the average relative density of all samples above 99%. The application of pressure combined with high temperature allowed to remove the internal closed porosity. This can be clearly observed in Figure 6, where the sinter-HIPed sample micrographs (Figure 6C and D) do not feature relevant macro-porosity as in the sintered samples (Figure 6A and B). At both stages, fine and coarse grains can be observed, which are due to the microstructure of the powder employed and have been studied in previous works (Enneti et al., 2018; Mariani, Beltrami, et al., 2021).

Figure 7B displays the hardness values obtained from micro-indentation on longitudinal section of sintered and sinter-HIPed samples. The main

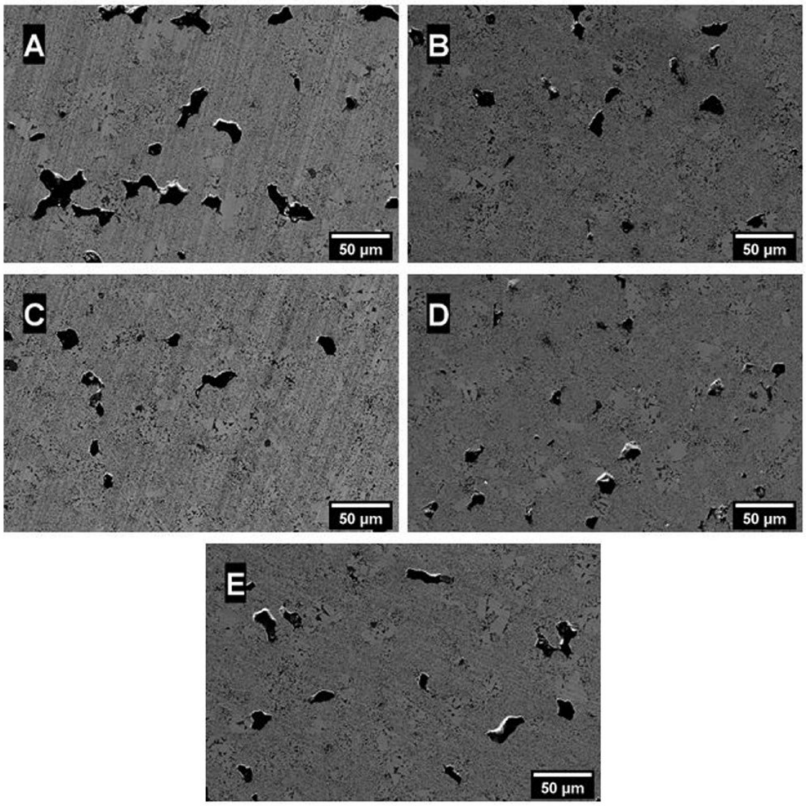

Figure 4. SEM micrographs of the sintered samples transverse sections. In order: (A) 50_60; (B) 50_75; (C) 100_60; (D) 100_75; (E) 100_90.

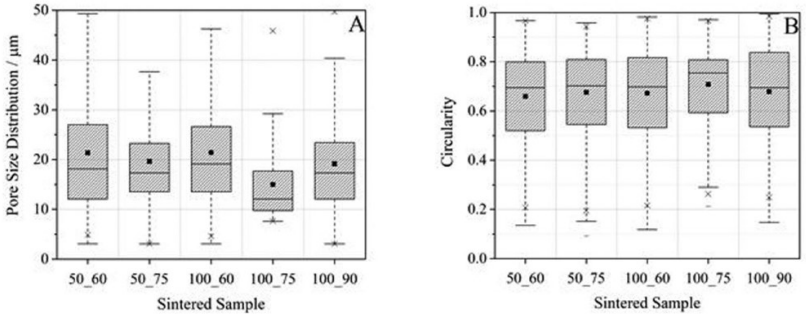

Figure 5. Pore size (A) and circularity (B) values distributions of the sintered samples obtained from the combination of LT = 50/100 µm and BS = 60/75/90%.

difference stands in the presence of values below 1100 HV of some samples, which are due to residual porosity that may produce an enlargement of the indented track. Sinter-HIPed components feature an extremely limited porosity, thus the risk of pore-affected measurements is reduced, and lower values close to 1200 HV are likely generated by cobalt pools that are observed throughout the microstructure of all the samples. Effects of the presence of graphitized carbon in the microstructure could be excluded since relevant differences were not detected in between five printing parameters combinations and among sintered and sinter-HIPed specimens, as can be seen from Table 6. The risk could have arisen from the incomplete burnout of the polymer during debinding in inert atmosphere (Lecis et al., 2021), however the process was effective in removing the organic binder prior to densification to an extent sufficient at avoiding the risk of printing-dependent microstructural defects or anomalies.

Once again, distinctions in between the tested printing combinations were not detected at the microstructural level, coherently with the homogeneity observed in the microstructural features, while macroscopic geometrical inaccuracies can be easily observed with higher LT and BS, as can be seen in Figure 8, where the samples with the lowest and largest amount of binder at each layer are presented (50_60 and 100_90, respectively).

4. Conclusions

The work describes the effects of the pivotal parameters for the organic binder distribution within binder jetted specimens, i.e. the layer thickness (LT) and the binder saturation (BS), on the geometrical accuracy and microstructural properties. The tested conditions include two LT (50 and

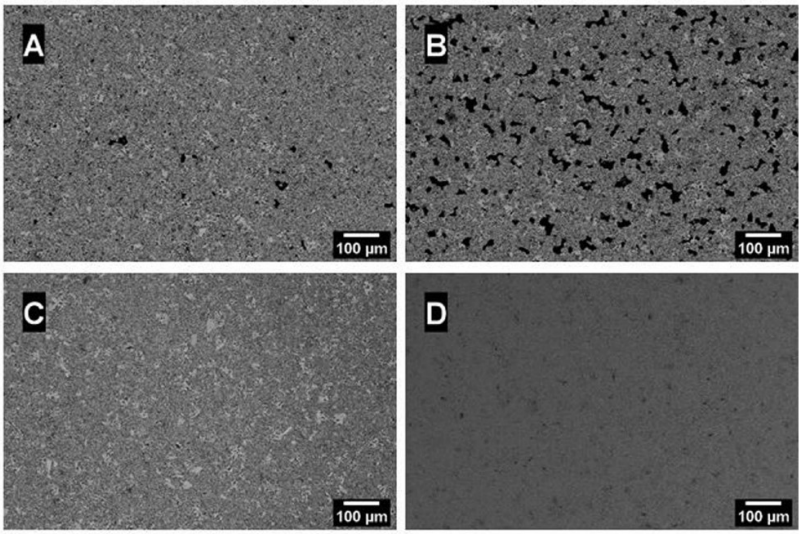

Figure 6. SEM micrographs of sintered longitudinal (A) and transverse (B) polished section surfaces and of sinter-HIPed longitudinal (C) and transverse (D) polished section surfaces of the 50_60 specimen.

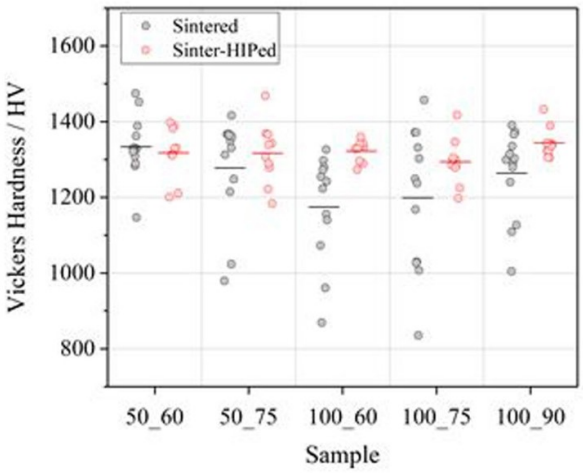

Figure 7. Vickers hardness values measured on sintered (gray) and sinter-HIPed (red) samples obtained from the combination of LT = 50/100 µm and BS = 60/75/90%.

Table 6. Average carbon content values (%) before and after sinter-HIP treatment.

	Process step	50_60	50_75	100_60	100_75	100_90
Carbon content/ wt.%	Sintering	5.54 ± 0.01	5.51 ± 0.02	5.56 ± 0.02	5.52 ± 0.03	5.53 ± 0.04
	Sinter-HIP	5.54 ± 0.03	5.52 ± 0.01	5.57 ± 0.12	5.55 ± 0.06	5.54 ± 0.01

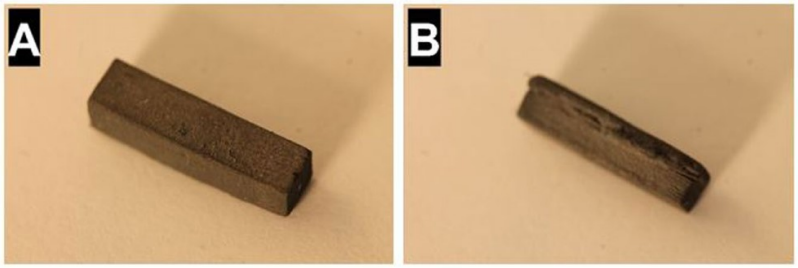

Figure 8. Side view of sinter-HIPed specimens: (A) 50_60; (B) 100_90.

100 µm) and three BS levels (60, 75 and 90%). The material employed is tungsten carbide with a 12 wt.% Co matrix powder, obtained from plasma spheroidization.

The analyses performed at the different stages of the process have underlined that:

- both LT and BS strongly affect the reliability of the shaping phase, given its dependence on the distribution of the binder within the powder bed, highlighting improved green parts quality for lower values of both parameters;
- after sintering and sinter-HIP, the differences at the microstructural level are minimised, thus the correlated mechanical properties are comparable for all the tested conditions, which is certainly advantageous in terms of flexibility of the production cycle.

In conclusion, the main effect of the printing parameters choice on the finished products is that on their level of geometrical accuracy. This is of pivotal importance for commercialisation because the huge advantage of producing this class of material from AM would be obtaining complex design and details without the need of surface material removal.

Acknowledgments

Authors would like to acknowledge the "Functional Sintered Materials (Funtasma)" Interdepartmental Laboratory of Politecnico di Milano, where this research activity was developed. Support by the Italian Ministry for Education, University and Research through the project Department of Excellence LIS4.0 (Integrated Laboratory for Lightweight e Smart Structures) is also acknowledged. Finally, authors would like to acknowledge the support given by HI.Lab for the preparation and analysis of the sintered and sinter-HIP samples.

Disclosure statement

No potential conflict of interest was reported by the authors.

References

Aramian, A., Razavi, S. M. J., Sadeghian, Z., & Berto, F. (2020). A review of additive manufacturing of cermets. *Additive Manufacturing*, *33*, 101130. https://doi.org/10.1016/j.addma.2020.101130.

Arganda-Carreras, I., Kaynig, V., Rueden, C., Eliceiri, K. W., Schindelin, J., Cardona, A., & Seung, H. S. (2017). Trainable Weka Segmentation: A machine learning tool for microscopy pixel classification. *Bioinformatics (Oxford, England)*, *33*(15), 2424–2426. https://doi.org/10.1093/bioinformatics/btx180.

Barthel, B., Janas, F., & Wieland, S. (2021). Powder condition and spreading parameter impact on green and sintered density in metal binder jetting. *Powder Metallurgy*, *2021*, 1–9. https://doi.org/10.1080/00325899.2021.1912923.

Campanelli, S. L., Contuzzi, N., Posa, P., & Angelastro, A. (2019). Printability and microstructure of selective laser melting of WC/Co/Cr powder. *Materials (Basel)*, *12*(15), 2397. https://doi.org/10.3390/ma12152397.

Carreño-Morelli, E., Alveen, P., Moseley, S., Rodriguez-Arbaizar, M., & Cardoso, K. (2020). Three-dimensional printing of hard materials. *International Journal of Refractory Metals and Hard Materials*, *87*, 105110. https://doi.org/10.1016/j.ijrmhm.2019.105110.

Chen, J., Huang, M., Fang, Z. Z., Koopman, M., Liu, W., Deng, X., … Wang, Z. (2019). Microstructure analysis of high density WC-Co composite prepared by one step selective laser melting. *International Journal of Refractory Metals and Hard Materials*, *84*, 104980. https://doi.org/10.1016/j.ijrmhm.2019.104980.

Chun, S. Y., Kim, T., Ye, B., Jeong, B., Jin Lee, M., Lee, D. H., … Kim, H.-D. (2020). Capillary pressure and saturation of pore-controlled granules for powder bed binder jetting. *Applied Surface Science*, *515*, 145979. https://doi.org/10.1016/j.apsusc.2020.145979.

Cramer, C. L., Aguirre, T. G., Wieber, N. R., Lowden, R. A., Trofimov, A. A., Wang, H., … Elliott, A. M. (2020). Binder jet printed WC infiltrated with pre-made melt of WC and Co. *International Journal of Refractory Metals and Hard Materials*, *87*, 105137. https://doi.org/10.1016/j.ijrmhm.2019.105137.

Cramer, C. L., Nandwana, P., Lowden, R. A., & Elliott, A. M. (2019). Infiltration studies of additive manufacture of WC with Co using binder jetting and pressureless melt method. *Additive Manufacturing*, *28*, 333–343. https://doi.org/10.1016/j.addma.2019.04.009.

Cramer, C. L., Wieber, N. R., Aguirre, T. G., Lowden, R. A., & Elliott, A. M. (2019). Shape retention and infiltration height in complex WC-Co parts made via binder jet of WC with subsequent Co melt infiltration. *Additive Manufacturing*, *29*, 100828. https://doi.org/10.1016/j.addma.2019.100828.

Cui, S., Lu, S., Tieu, K., Meenashisundaram, G. K., Wang, L., Li, X., … Li, W. (2021). Detailed assessments of tribological properties of binder jetting printed stainless steel and tungsten carbide infiltrated with bronze. *Wear*, *477*, 203788. https://doi.org/10.1016/j.wear.2021.203788.

Davoren, B., Sacks, N., & Theron, M. (2020). Laser engineered net shaping of WC-9.2wt%Ni alloys: A feasibility study. *International Journal of Refractory Metals and Hard Materials*, *86*, 105136. https://doi.org/10.1016/j.ijrmhm.2019.105136.

Eguiluz, A., Ferr, A., Yus, J., Ferrari, B. (2021). Dispersion of Ni nanoparticles into Ti (C, N) colloidal fi laments for 3D printing by FFF. *Open Ceramics*, *5*, 100064. https://doi.org/10.1016/j.oceram.2021.100064.

Enneti, R. K., & Prough, K. C. (2019a). Effect of binder saturation and powder layer thickness on the green strength of the binder jet 3D printing (BJ3DP) WC-12%Co powders. *International Journal of Refractory Metals and Hard Materials*, *84*, 104991. https://doi.org/10.1016/j.ijrmhm.2019.104991.

Enneti, R. K., & Prough, K. C. (2019b). Wear properties of sintered WC-12%Co processed via Binder Jet 3D Printing (BJ3DP). *International Journal of Refractory Metals and Hard Materials*, *78*, 228–232. https://doi.org/10.1016/j.ijrmhm.2018.10.003.

Enneti, R. K., Prough, K. C., Wolfe, T. A., Klein, A., Studley, N., & Trasorras, J. L. (2018). Sintering of WC-12%Co processed by binder jet 3D printing (BJ3DP) technology. *International Journal of Refractory Metals and Hard Materials*, *71*, 28–35. https://doi.org/10.1016/j.ijrmhm.2017.10.023.

Gao, W., Zhang, Y., Ramanujan, D., Ramani, K., Chen, Y., Williams, C. B., … Zavattieri, P. D. (2015). The status, challenges, and future of additive manufacturing in engineering. *Computer-Aided Design*, *69*, 65–89. https://doi.org/10.1016/j.cad.2015.04.001.

Grigoriev, S., Tarasova, T., Gusarov, A., Khmyrov, R., & Egorov, S. (2019). Possibilities of manufacturing products from cermet compositions using nanoscale powders by additive manufacturing methods. *Materials (Basel)*, *12*(20), 3425. https://doi.org/10.3390/ma12203425.

Gu, D., Hagedorn, Y. C., Meiners, W., Meng, G., Batista, R. J. S., Wissenbach, K., & Poprawe, R. (2012). Densification behavior, microstructure evolution, and wear performance of selective laser melting processed commercially pure titanium. *Acta Materialia*, *60*(9), 3849–3860. https://doi.org/10.1016/j.actamat.2012.04.006.

Jimenez, E. M., Ding, D., Su, L., Joshi, A. R., Singh, A., Reeja-Jayan, B., & Beuth, J. (2019). Parametric analysis to quantify process input influence on the printed densities of binder jetted alumina ceramics. *Additive Manufacturing*, *30*, 100864. https://doi.org/10.1016/j.addma.2019.100864.

Ku, N., Pittari, J. J., Kilczewski, S., & Kudzal, A. (2019). Additive manufacturing of cemented tungsten carbide with a cobalt-free alloy binder by selective laser melting for high-hardness applications. *JOM Journal of the Minerals Metals and Materials Society*, *71*(4), 1535–1542. https://doi.org/10.1007/s11837-019-03366-2.

Lecis, N., Mariani, M., Beltrami, R., Emanuelli, L., Casati, R., Vedani, M., & Molinari, A. (2021). Effects of process parameters, debinding and sintering on the microstructure of 316L stainless steel produced by binder jetting. *Materials Science and Engineering: A*, *828*, 142108. https://doi.org/10.1016/j.msea.2021.142108.

Lehmann, M., & Zaeh, M. F. (2019). *Process integrated production of wc-co tools with local cobalt gradient fabricated by binder jetting*Solid Free. Fabr. 2019 Proc. 30th Annu. Int. Solid Free. Fabr. Symp. - an Addit. Manuf. Conf. SFF 2019, Preprints, pp. 109–121. https://doi.org/10.20944/PREPRINTS202101.0497.V1.

Lengauer, W., Duretek, I., Fürst, M., Schwarz, V., Gonzalez-Gutierrez, J., Schuschnigg, S., … Morrison, V. (2019). Fabrication and properties of extrusion-based 3D-printed hardmetal and cermet components. *International Journal of Refractory Metals and Hard Materials*, *82*, 141–149. https://doi.org/10.1016/j.ijrmhm.2019.04.011.

Lin, D., Xu, J., Shan, Z., Chung, S. T., & Park, S. J. (2015). Fabrication of WC-Co cutting tool by powder injection molding. *International Journal of Precision Engineering and Manufacturing*, *16*(7), 1435–1439. https://doi.org/10.1007/s12541-015-0189-8.

Mao, Y., Li, J., Li, W., Cai, D., & Wei, Q. (2021). Binder jetting additive manufacturing of 316L stainless-steel green parts with high strength and low binder content: Binder preparation and process optimization. *Journal of Materials Processing Technology*, *291*, 117020. https://doi.org/10.1016/j.jmatprotec.2020.117020.

Mariani, M., Beltrami, R., Brusa, P., Galassi, C., Ardito, R., & Lecis, N. (2021). 3D printing of fine alumina powders by binder jetting. *Journal of the European Ceramic Society*, *41*(10), 5307–5315. https://doi.org/10.1016/j.jeurceramsoc.2021.04.006.

Mariani, M., Goncharov, I., Mariani, D., Pietro De Gaudenzi, G., Popovich, A., Lecis, N., & Vedani, M. (2021). Mechanical and microstructural characterization of WC-Co consolidated by binder jetting additive manufacturing. *International Journal of Refractory Metals and Hard Materials*, *100*, 105639. https://doi.org/10.1016/j.ijrmhm.2021.105639.

Mostafaei, A., De Vecchis, P. R., Kimes, K. A., Elhassid, D., & Chmielus, M. (2021). Effect of binder saturation and drying time on microstructure and resulting properties of sinter-HIP binder-jet 3D-printed WC-Co composites. *Additive Manufacturing*, *46*, 102128. https://doi.org/10.1016/j.addma.2021.102128.

Mostafaei, A., Elliott, A. M., Barnes, J. E., Li, F., Tan, W., Cramer, C. L., … Chmielus, M. (2021). Binder jet 3D printing—Process parameters, materials, properties, modeling, and challenges. *Progress in Materials Science*, *119*, 100707. https://doi.org/10.1016/j.pmatsci.2020.100707.

Mudanyi, R. K., Cramer, C. L., Elliott, A. M., Unocic, K. A., Guo, Q., & Kumar, D. (2021). W-ZrC composites prepared by reactive melt infiltration of Zr2Cu alloy into binder jet 3D printed WC preforms. *International Journal of Refractory Metals and Hard Materials*, *94*, 105411. https://doi.org/10.1016/j.ijrmhm.2020.105411.

Nandwana, P., Kannan, R., & Siddel, D. (2020). Microstructure evolution during binder jet additive manufacturing of H13 tool steel. *Additive Manufacturing*, *36*, 101534. https://doi.org/10.1016/j.addma.2020.101534.

Rishmawi, I., Salarian, M., & Vlasea, M. (2018). Tailoring green and sintered density of pure iron parts using binder jetting additive manufacturing. *Additive Manufacturing*, *24*, 508–520. https://doi.org/10.1016/j.addma.2018.10.015.

Seharing, A., Azman, A. H., & Abdullah, S. (2020). A review on integration of lightweight gradient lattice structures in additive manufacturing parts. *Advances in Mechanical Engineering*, *12*(6), 168781402091695. https://doi.org/10.1177/1687814020916951.

Wang, X. C., Laoui, T., Bonse, J., Kruth, J. P., Lauwers, B., & Froyen, L. (2002). Direct selective laser sintering of hard metal powders: Experimental study and simulation. *International Journal of Advanced Manufacturing Technology*, *19*(5), 351–357. https://doi.org/10.1007/s001700200024.